Med Biol Eng Comput (2013) 51:607–616
DOI 10.1007/s11517-012-1031-4

ORIGINAL ARTICLE

Computer simulation of three-dimensional plaque formation and progression in the carotid artery

Nenad Filipovic · Zhongzhao Teng · Milos Radovic · Igor Saveljic · Dimitris Fotiadis · Oberdan Parodi

Received: 5 March 2012 / Accepted: 30 December 2012 / Published online: 25 January 2013

Abstract Atherosclerosis is becoming the number one cause of death worldwide. In this study, three-dimensional computer model of plaque formation and development for human carotid artery is developed. The three-dimensional blood flow is described by the Navier–Stokes equation, together with the continuity equation. Mass transfer within the blood lumen and through the arterial wall is coupled with the blood flow and is modeled by a convection–diffusion equation. The low-density lipoproteins transports in lumen of the vessel and through the vessel tissue are coupled by Kedem–Katchalsky equations. The inflammatory process is modeled using three additional reaction–diffusion partial differential equations. Fluid–structure interaction is used to estimate effective wall stress analysis. Plaque growth functions for volume progression are correlated with shear stress and effective wall stress distribution. We choose two specific patients from MRI study with significant plaque progression. Plaque volume progression using three time points for baseline, 3- and 12-month follow up is fitted. Our results for plaque localization correspond to low shear stress zone and we fitted parameters from our model using nonlinear least-square method. Determination of plaque location and composition, and computer simulation of progression in time for a specific patient shows a potential benefit for the prediction of disease progression. The proof of validity of three-dimensional computer modeling in the evaluation of atherosclerotic plaque burden may shift the clinical information of MRI from morphological assessment toward a functional tool. Understanding and prediction of the evolution of atherosclerotic plaques either into vulnerable or stable plaques are major tasks for the medical community.

Keywords Atherosclerosis · Carotid artery · Plaque formation and progression · Computer modeling · MRI

1 Introduction

Atherosclerosis is an inflammatory disease. A prominent role of low-density lipoproteins (LDL) for inflammation in atherosclerosis is well known [11]. The process of inflammation starts with penetration of LDL in the intima. This penetration is followed by leucocyte recruitment in the intima. It may participate in formation of the fatty streak, the initial lesion of atherosclerosis and then in formation of a plaque [12].

The blood flow and its influence to arterial wall have been studied for decades. Computational techniques and simulations have been developed to understand the blood flow dynamics and the mechanical behavior of the arterial wall. Several mathematical models have recently been set up for the transport of macromolecules, such as LDPs, from the arterial lumen to the arterial wall and inside the wall [15, 19, 22]. These models are usually classified into three categories according to the level of description of the arterial wall. The simplest model is called the wall-free model, since in this model, the arterial wall is simply

N. Filipovic (✉) · M. Radovic · I. Saveljic
University of Kragujevac, Kragujevac, Serbia
e-mail: fica@kg.ac.rs

Z. Teng
University of Cambridge, Cambridge, UK

D. Fotiadis
University of Ioannina, Ioannina, Greece

O. Parodi
National Research Council Pisa, Pisa, Italy

described by means of an appropriate boundary condition. Kaazempur-Mofrad and Ethier [7] simulated the mass transport in a realistic human right coronary artery and Wada et al. [20] used a wall-free model to study the concentration polarization phenomenon. The wall-free model does not provide any information on the transmural flow and solute dynamics in the arterial wall. The fluid-wall models that can be either single-layer or multilayer account for the solute dynamics not only in the lumen but also in the arterial wall. Stangeby and Ethier [18] analyzed the wall as single-layer porous medium and solved the coupled luminal blood flow and transmural fluid flow using Brinkman's equations. Sun et al. used single and Al and Vafai [1] used multilayer models which represent intima and media separately. Olgac et al. [14] used a three-pore model for LDL transport.

The early stage of the inflammatory disease is the result of interaction between plasma LDL that filtrate through endothelium into the intima, cellular components (monocytes/macrophages, endothelial cells and smooth muscle cells) and the extracellular matrix of the arterial wall [16].

Our working hypotheses are:

The local arterial wall volume increases as the result of newly formed foam cells.

Monocytes evolve in macrophages which phagocyte oxidized LDL and in foam cells by massive ingestion of oxidized LDL. Transformation of macrophages into foam cells contribute to the recruitment of new monocytes. It yields the secretion of a pro-inflammatory signal (cytokines). It is a self-supportive inflammatory reaction. Newly formed foam cells are responsible for the local volume increase. Under a local incompressibility assumption, when foam cells are created, the intima volume is locally increasing. We further assume that arterial wall permeability increase in the zone of low wall shear stress (WSS) and elastic property of the arterial wall for fluid–structure interaction problem.

In what follows, we describe mass transport of LDL through the wall and a simplified inflammatory process by coupling the Navier–Stokes equation, the Darcy equation for blood filtration and Kedem–Katchalsky equations [9, 8], for the solute and flux exchanges between the lumen and intima. A system of three additional reaction–diffusion equations is formed for the inflammatory process and lesion growth in the intima. Fluid–structure interaction is used for effective wall stress analysis. Arbitrary Lagrangian–Eulerian (ALE) formulation is used for mesh moving. The procedure for fitting of plaque-growing function which depends on shear stress and effective wall stress is developed. Presentation of the basic equations is followed by results of modeling the plaque development in human carotid artery for baseline, 3 and 12 months. Finally, we discuss and summarize the computational results.

2 Materials and methods

Fifty patients with carotid atherosclerotic disease underwent high-resolution MRI of their carotid arteries in a 1.5-T MRI system (Signa HDx GE Healthcare, Waukesha, WI) with a 4-channel phased array neck coil (PACC, Machnet BV, Elde, The Netherlands) [17]. The study protocol was reviewed and approved by the regional research ethics committee and all patients gave written informed consent.

After an initial coronal localizer sequence, axial 2D time-of-flight (TOF) MR angiography was performed to identify the location of the carotid bifurcation and the region of maximum stenosis. The following sequences were used to depict the various contents within the plaque structure: T1 weighted (repetition time/echo time: 1 × RR/7.8 ms) with fat saturation; T2 weighted (repetition time/echo time: 2 × RR/100 ms) with fat saturation; proton density (PD) weighted (repetition time/echo time: 2 × RR/7.8 ms) with fat saturation; short tau inversion recovery (STIR) (repetition time/echo time/inversion time: 2 × RR/46/150 ms). The field of view was 10 cm × 10 cm and matrix size 256 × 256. The in-plane spatial resolution achieved was of the order of 0.39 mm × 0.39 mm × 3 mm. Plaque components, i.e., lipid and fibrous tissue were manually delineated by two experienced MR readers using CMR Tools (London, UK) with previously published criteria [17]. Two specific patients with high plaque progression were chosen. We did manual segmentation of plaque components, such as fibrous cap and chronic hemorrhage tissue, calcium and PH, using carotid MR images.

The fundamental equations for the LDL transport through blood vessel lumen and vessel wall and for plaque development are given. In addition, procedure for estimation of plaque growth function is described. The three-dimensional blood flow in lumen domain is modeled by the Navier–Stokes equations, together with the continuity equation of incompressible fluid:

$$\partial_t \mathbf{u}_l - \mu \nabla^2 \mathbf{u}_l + \rho(\mathbf{u}_l \cdot \nabla)\mathbf{u}_l + \nabla p_l = 0 \quad (1)$$

$$\nabla \mathbf{u}_l = 0 \quad (2)$$

where $\mathbf{u}_l$ is blood velocity in the lumen, p_l is pressure, μ is the dynamic viscosity of blood, and ρ is blood density [10].

Mass transfer in the blood lumen is coupled with the blood flow by a convection–diffusion equation,

$$\nabla \cdot (-D_l \nabla c_l + c_l \mathbf{u}_l) = 0 \quad (3)$$

in the fluid domain, where c_l is the solute concentration in the blood lumen, and D_l is the solute diffusivity in the lumen. Mass transfer in the arterial wall is coupled to the transmural flow and modeled by a convection–diffusion-reaction equation as follows

$$\nabla \cdot (-D_w \nabla c_w + k c_w \mathbf{u}_w) = r_w c_w \quad (4)$$

where c_w is the solute concentration and D_w is the solute diffusivity in the arterial wall; $\mathbf{u}_w$ is blood velocity in the wall, k is the solute lag coefficient, and r_w is the consumption rate constant. The LDL transports in lumen and in the vessel wall are coupled by the Kedem–Katchalsky equations:

$$J_v = L_p(\Delta p - \sigma_d \Delta \pi) \quad (5)$$

$$J_s = P\Delta c + (1 - \sigma_f) J_v \bar{c} \quad (6)$$

where L_p is hydraulic conductivity of the endothelium; Δc is the solute concentration difference, Δp is the pressure drop and $\Delta \pi$ is the oncotic pressure difference, all across the endothelium; σ_d is the osmotic reflection coefficient, σ_f is the solvent reflection coefficient, P is the solute endothelial permeability, and $\bar{c}$ is the mean endothelial concentration. The first term in Kedem–Katchalsky equations $P\Delta c$ of the right hand side in (Eq. 6) defines the diffusive flux across the endothelium, while the second term $(1 - \sigma_f) J_v \bar{c}$ defines the convective flux. Only the oncotic pressure difference $\Delta \pi$ is neglected in our simulations because of decoupling the fluid dynamics from solute dynamics. We assume that term P is a function of the WSS as higher permeability to areas with low shear stress $P = a_0 \log\left(1 + \frac{a_1}{\mathrm{WSS} + a_2}\right)$, where a_0, a_1 and a_2 are positive parameters.

The above governing equations are transformed into a finite element system of incremental–iterative equations and solved over time steps.

The atherosclerotic process starts with the accumulation of LDL in the intima, where part of them are oxidized and become pathological. To remove the oxidized particles, circulating immune cells (e.g., monocytes) are recruited. Once in the intima, the monocytes differentiate and become macrophages that phagocyte the oxidized LDL. Fatty macrophages then transform into foam cells. Foam cells are responsible for the growth of a subendothelial plaque which eventually emerges in the artery lumen.

The inflammatory process is modeled using three additional reaction–diffusion partial differential equations [5] [4]:

$$\begin{aligned} \partial_t O &= d_1 \Delta O - k_1 O \cdot M \\ \partial_t M + \mathrm{div}(v_w M) &= d_2 \Delta M - k_1 O \cdot M + S/(1+S) \\ \partial_t S &= d_3 \Delta S - \lambda S + k_1 O \cdot M + \gamma (O - O^{\mathrm{thr}}) \end{aligned} \quad (7)$$

where O is the oxidized LDL in the wall, M and S are concentrations in the intima of macrophages and cytokines, respectively; d_1, d_2, d_3 are the corresponding diffusion coefficients; λ and γ are degradation and LDL oxidized detection coefficients; v_w is the inflammatory velocity of plaque growth, which satisfies Darcy's law and incompressibility continuity equation [3]:

$$\mathbf{v}_w - \nabla \cdot (p_w) = k_1 O \cdot M \quad (8)$$

$$\nabla \mathbf{v}_w = 0 \quad (9)$$

in the wall domain. Here, p_w is the pressure in the arterial wall.

To follow change of the vessel wall geometry during plaque growth, a 3D mesh-moving algorithm ALE is applied [3].

2.1 Mesh-moving algorithm

The governing equations, which include the Navier–Stokes equations of balance of linear momentum and the continuity equation, can be written in the ALE formulation as [3].

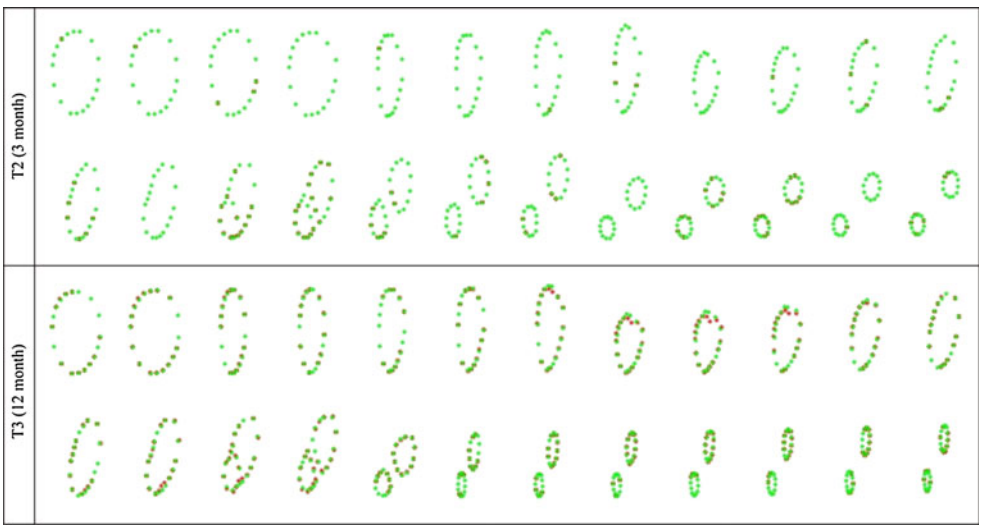

Fig. 1 Simulated contour plots compared with target contours at time steps $T2$ (3 months) and $T3$ (12 months). *Green* simulated contours, *red* target contours (color figure online)

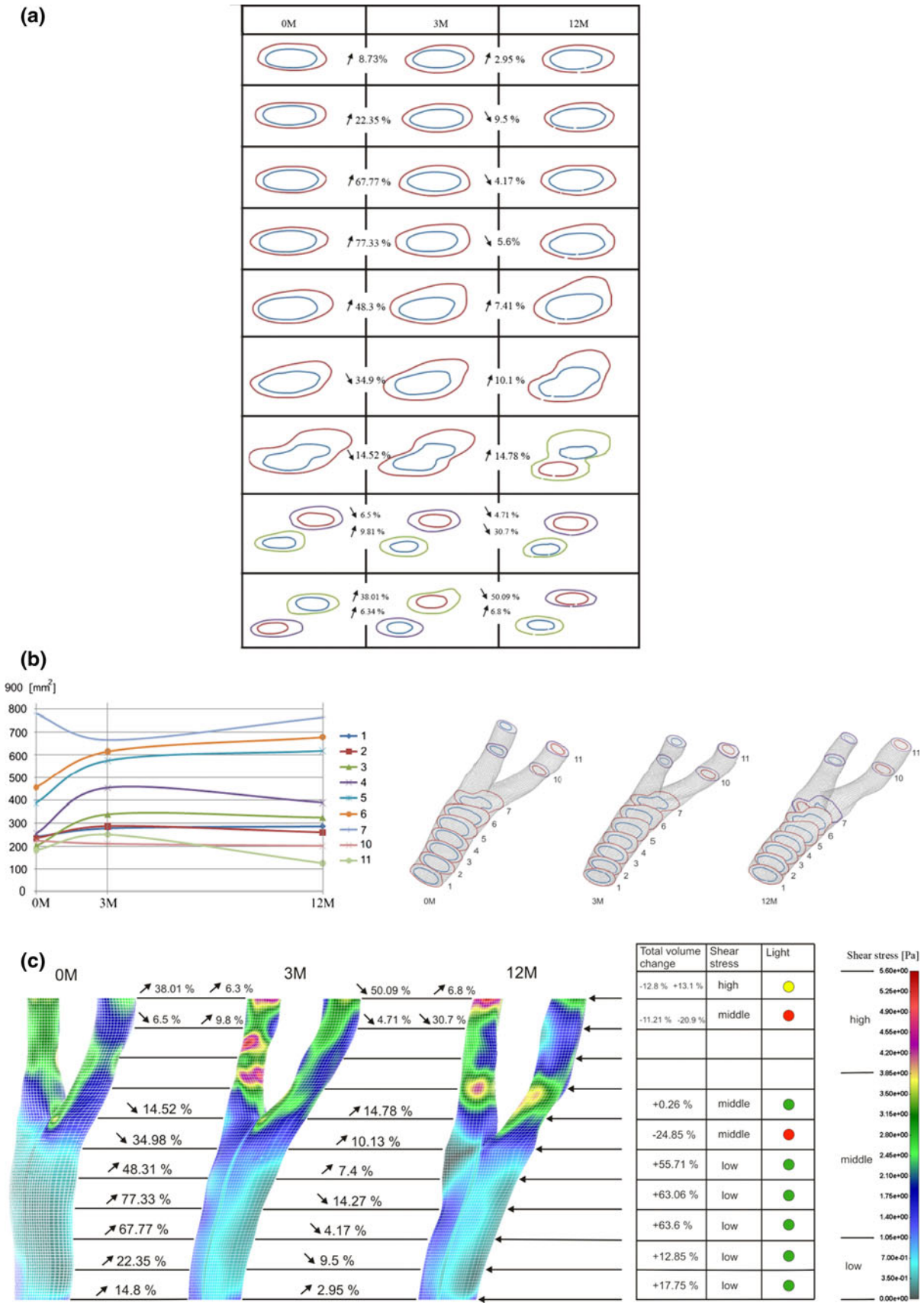
(a)
0M
3M
12M
8.73%
2.95 %
22.35 %
9.5 %
67.77 %
4.17 %
77.33 %
5.6%
48.3 %
7.41 %
34.9 %
10.1 %
14.52 %
14.78 %
6.5 %
9.81 %
4.71 %
30.7 %
38.01 %
6.34 %
50.09 %
6.8 %
(b)
900 [mm²]
800
700
600
500
400
300
200
100
0
0M
3M
12M
1
2
3
4
5
6
7
10
11
(c)
0M
3M
12M
38.01 %
6.3 %
6.5 %
9.8 %
14.52 %
34.98 %
48.31 %
77.33 %
67.77 %
22.35 %
14.8 %
50.09 %
6.8 %
4.71 %
30.7 %
14.78 %
10.13 %
7.4 %
14.27 %
4.17 %
9.5 %
2.95 %
Total volume change
Shear stress
Light
-12.8 % +13.1 %
high
-11.21 % -20.9 %
middle
+0.26 %
middle
-24.85 %
middle
+55.71 %
low
+63.06 %
low
+63.6 %
low
+12.85 %
low
+17.75 %
low
Shear stress [Pa]
high
middle
low

◀ **Fig. 2** **a** Cross-section areas changes for patient #1 (area between the inner and the outer wall). **b** Cross-section areas versus time (0, 3 and 12 months) for patient #1. **c** Correlation of cross-sections changes with wall shear stress for patient #1

$$\rho[\partial_t \mathbf{u}^* + (\mathbf{u} - \mathbf{u}^{\mathrm{m}}) \cdot \nabla \mathbf{u}] = -\nabla p + \mu \nabla^2 \mathbf{u} + \mathbf{f}^{\mathrm{B}} \tag{10}$$

$$\nabla \mathbf{u} = 0 \tag{11}$$

where v_i and v_i^{m} are the velocity components of a generic fluid particle and of the point on the moving mesh occupied by the fluid particle, respectively; ρ is fluid density, p is fluid pressure, μ is dynamic viscosity, and f_i^{B} are the body force components. The symbol "*" denotes the mesh-referential time derivative, i.e., the time derivative at a considered point on the mesh,

$$()^* = \frac{\partial()}{\partial t}\Big|_{\xi_i = \mathrm{const}} \tag{12}$$

and the symbol "$_{,i}$" denotes partial derivative, i.e.,

$$()_{,i} = \frac{\partial()}{\partial x_i}. \tag{13}$$

We use x_i and ξ_i as Cartesian coordinates of a generic particle in space and of the corresponding point on the mesh, respectively. The repeated index means summation, from 1 to 3, i.e., $j = 1, 2, 3$ in Eq. (10), and $i = 1, 2, 3$ in Eq. (11). In deriving Eq. (10), we used the following expression for the material derivative (corresponding to a fixed material point) $\mathrm{D}(\rho v_i)/\mathrm{D}t$,

$$\frac{\mathrm{D}(\rho v_i)}{\mathrm{D}t} = \frac{\partial(\rho v_i)}{\partial t}\Big|_{\xi} + (v_j - v_j^m)\frac{\partial(\rho v_j)}{\partial x_i} \tag{14}$$

The derivatives on the right-hand side correspond to a generic point on the mesh, with the mesh-referential derivative and the convective term.

Using the linearization (14), we obtain from (10) and (11) the system of ordinary differential equations in the form

$${}^t\mathbf{M}_{(1)}\mathbf{U}^* + {}^t\mathbf{K}_{(1)uu}\Delta\mathbf{U} + {}^t\mathbf{K}_{up}\Delta\mathbf{P} = {}^{t+\Delta t}\mathbf{F}_{(1)} - {}^t\mathbf{F}_{(1)} \tag{15}$$

and

$${}^t\mathbf{M}_{(2)}\mathbf{U}^* + {}^t\mathbf{K}_{(2)uu}\Delta\mathbf{U} = {}^{t+\Delta t}\mathbf{F}_{(2)} - {}^t\mathbf{F}_{(2)}. \tag{16}$$

The matrices and vectors follow from the volume and surface integrals given in [3].

2.2 Fluid–structure interaction

For fluid–structure interaction problem, the wall displacements can be large, hence, the problem becomes geometrically nonlinear. In addition, the tissue of blood vessels has nonlinear constitutive laws, leading to materially nonlinear finite element formulation. For a nonlinear wall tissue problem, the incremental–iterative equation is using:

$${}^{n+1}\hat{\mathbf{K}}_{\mathrm{tissue}}^{(i-1)}\,\Delta\mathbf{U}_{\mathrm{tissue}}^{(i)} = {}^{n+1}\hat{\mathbf{F}}^{(i-1)} - {}^{n+1}\mathbf{F}^{\mathrm{int(i-1)}} \tag{17}$$

where $\Delta\mathbf{U}_{\mathrm{tissue}}^{(i)}$ are the nodal displacement increments for the iteration 'i', and the system matrix ${}^{n+1}\hat{\mathbf{K}}_{\mathrm{tissue}}^{(i-1)}$, the force vector ${}^{n+1}\hat{\mathbf{F}}^{(i-1)}$ and the vector of internal forces ${}^{n+1}\mathbf{F}^{\mathrm{int(i-1)}}$ correspond to the previous iteration, n is the current time step.

The geometrically linear part of the stiffness matrix, $\left({}^{n+1}\mathbf{K}_L\right)_{\mathrm{tissue}}^{(i-1)}$, and nodal force vector, ${}^{n+1}\mathbf{F}^{\mathrm{int(i-1)}}$, are defined:

$$\left({}^{n+1}\mathbf{K}_L\right)_{\mathrm{tissue}}^{(i-1)} = \int_V \mathbf{B}_L^T\, {}^{n+1}\mathbf{C}_{\mathrm{tissue}}^{(i-1)}\mathbf{B}_L \mathrm{d}V, \quad \left({}^{n+1}\mathbf{F}^{\mathrm{int}}\right)^{(i-1)} = \int_V \mathbf{B}_L^T\, {}^{n+1}\boldsymbol{\sigma}^{(i-1)}\mathrm{d}V \tag{18}$$

where the consistent tangent constitutive matrix ${}^{n+1}\mathbf{C}_{\mathrm{tissue}}^{(i-1)}$ of tissue and the stresses at the end of time step ${}^{n+1}\boldsymbol{\sigma}^{(i-1)}$ depend on the material model used. $\mathbf{B}_{\mathrm{L}}$ is the linear strain–displacement matrix. Calculation of the matrix ${}^{n+1}\mathbf{C}_{\mathrm{tissue}}^{(i-1)}$ and the stresses ${}^{n+1}\boldsymbol{\sigma}^{(i-1)}$ for the tissue material models are performed at each iteration.

The overall strategy of fluid–structure interaction adopted here consists of the following steps [10].

a. For the current geometry of the blood vessel, determine blood flow (with use of the ALE formulation when the wall displacements are large). Wall velocities at the common blood—blood vessel surface are taken as the boundary condition for the fluid.
b. Calculate the loads, arising from the blood, which act on the walls.
c. Determine deformation of the walls taking the current loads from the blood.
d. Check for the overall convergence which includes fluid and solid. If convergence is reached, go to the next time step. Otherwise, go to step (a).
e. Update blood domain geometry and velocities at the common solid–fluid boundary for the new calculation of the blood flow. In case of large wall displacements, update the FE mesh for the blood flow domain. Go to step (a).

2.3 Fitting procedure for plaque volume growing function

For plaque volume growing, a fitting procedure for growth function which takes into account change of the coordinates, shear stress as well as effective wall stress data from fluid–structure interaction calculation is developed.

In this methodology, we used three known times $T1$, $T2$ and $T3$ [21] for estimation of plaque volume growth.

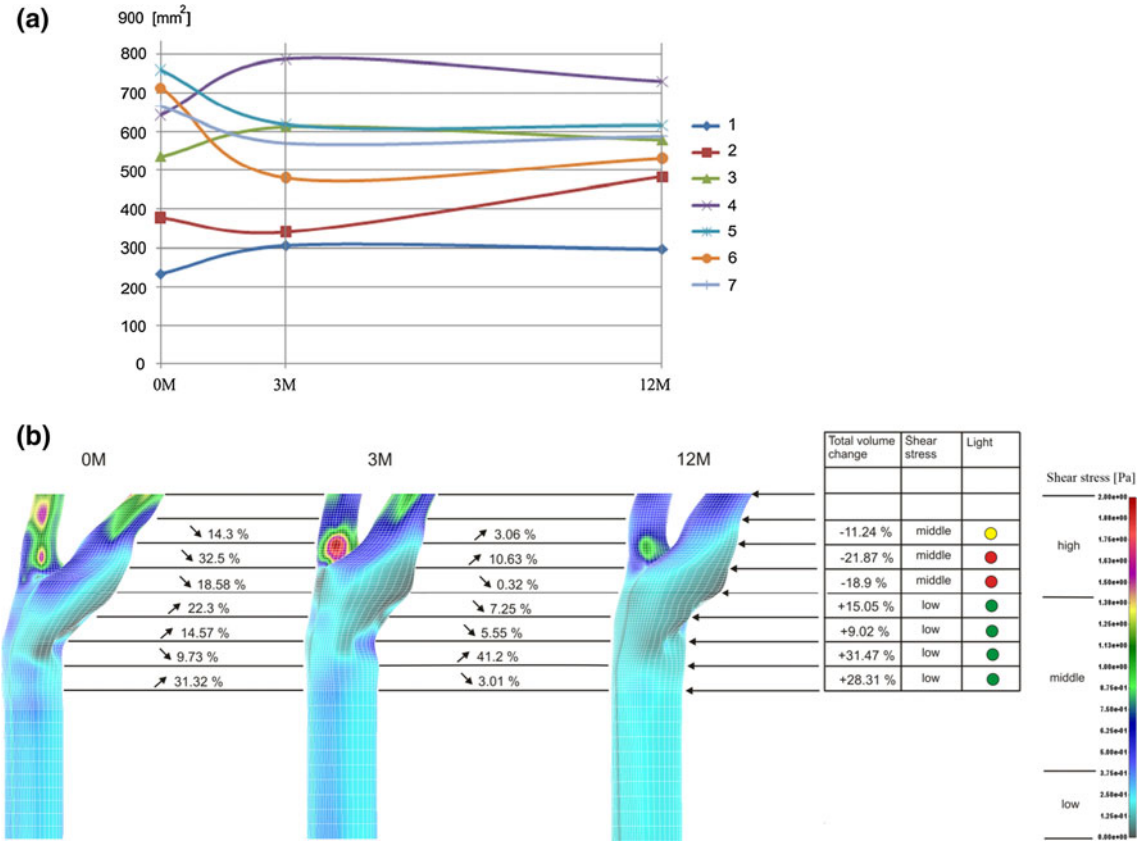

Fig. 3 **a** Cross-section areas versus time (0, 3 and 12 months) for patient #2. **b** Correlation of cross-section areas changes with wall shear stress for patient #2

Starting from the plaque geometry at $T1$, we used three different growth functions to simulate plaque progression and tried to reach the best agreement with plaque geometry obtained from image reconstruction at $T2$ and $T3$:

- GF1-growth function which uses nodal coordinates data only,
- GF2-growth function which uses nodal coordinates and shear stress data,
- GF3-growth function which uses nodal coordinates, shear stress and solid stress data.

These growth functions as well as the fitting procedure are described in detail in "Appendix".

Overlapping contour plots of the target and simulated results for time steps $T2$ and $T3$ is presented in Fig. 1.

3 Results

We compared changes in the cross-section areas for different patients with carotid artery progression. From 50 patients, we choose two with significant evidence of MR plaque progression to estimate parameter for our model of plaque formation and development. From MR slices, we segmented the inner and outer wall at nine cross-sections for baseline, 3 and 12 months. Segmented data for patient #1 are presented in Fig. 2a. Trends for increasing or decreasing cross-section areas versus time for patient #1 have been shown in Fig. 2b. It can be seen that almost all cross-section areas are increasing during follow-up time. For same patient, the correlation with WSS zones is shown in Fig. 2c. We used three categories as colors for the light: red denotes large decreasing in the cross-section area changes and middle WSS, yellow denotes small decrease in the cross-section area changes and middle WSS, while increase in the cross-section area changes and low WSS is denoted by green. Obviously from Fig. 2c, it can be concluded that there is a significant correlation with large increase in the cross-section areas and low WSS for patient #1. Similar analysis was done with patient #2. Cross-section areas versus time (0, 3 and 12 months) for patient #2 has been shown in Fig. 3a. Green light which denotes large increasing in the cross-section area changes and low WSS also is mostly dominant for patient #2 (Fig. 3b).

The different material properties for patient #1 have been shown in Fig. 4a, b. There are three different parts in

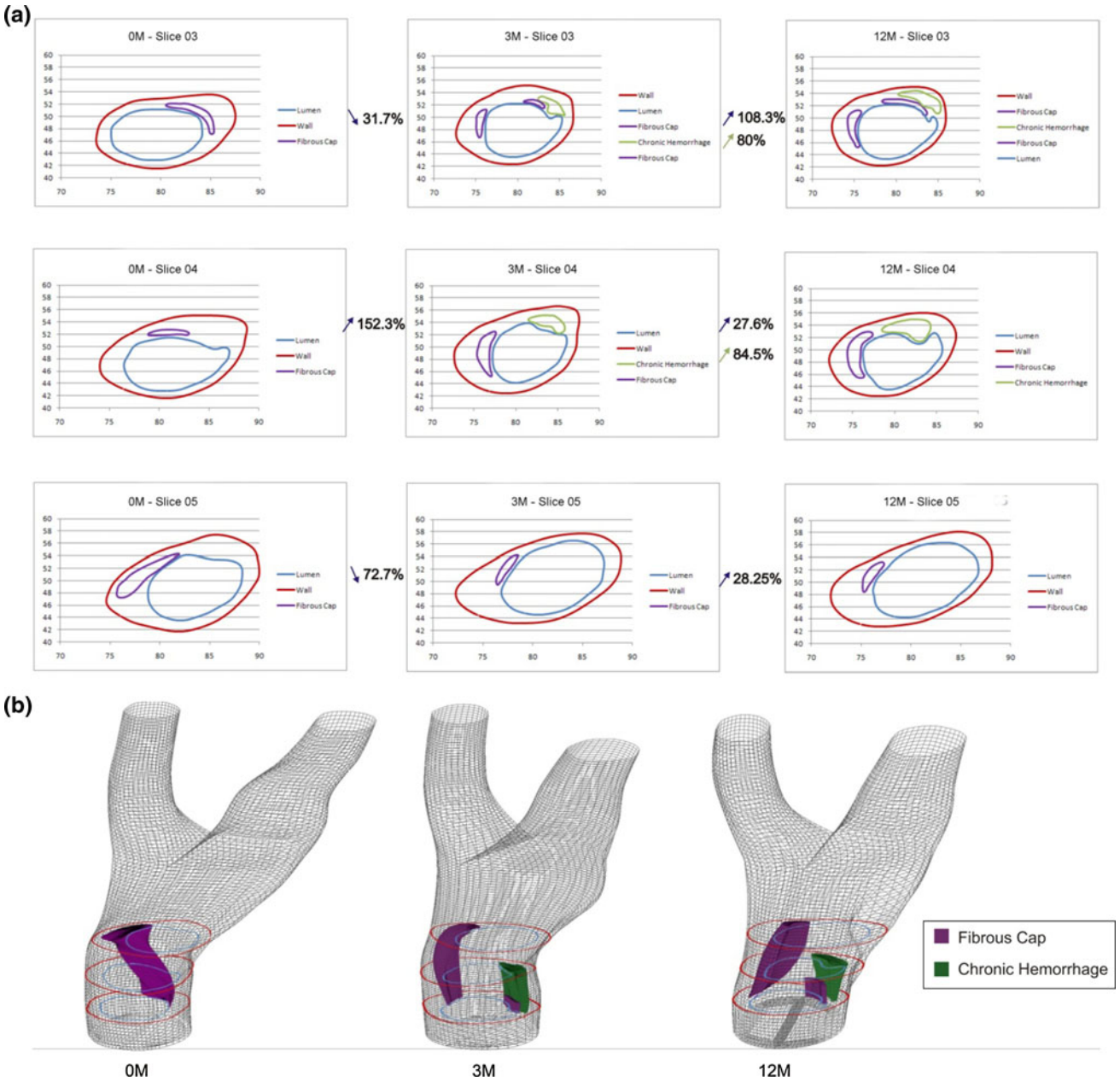

Fig. 4 **a** Different material properties for a specific patient #1 for follow-up study. **b** 3D presentation of plaque composition and different material properties for patient #1

the carotid arterial wall and Young's elasticity modules: artery tissue $E = 3.0e^6$ Pa, fibrous cap $E = 6.0e^6$ Pa, subacute hemorrhage $E = 4.5e^6$ Pa.

Effective wall stress for three different times (0, 3, and 12 months) at the maximum peak systole is presented in Fig. 5.

Volume of the plaque progression obtained from MRI system was fitted by employing a nonlinear least-square analysis [2], to determine material parameters in equations of Sect. 2. The fitted numerical parameters are given in Table 1.

4 Discussion

A three-dimensional computer model for plaque formation coupled with the LDL transport within artery and through the vessel wall is presented. The governing partial differential equations for plaque formation rely on the mass balance and Darcy's law in the domain of plaque development. The Navier–Stokes equations and diffusion equations are used for the LDL transport within the arterial lumen; and the transport–diffusion-reaction equations are employed for the transmural mass transport,

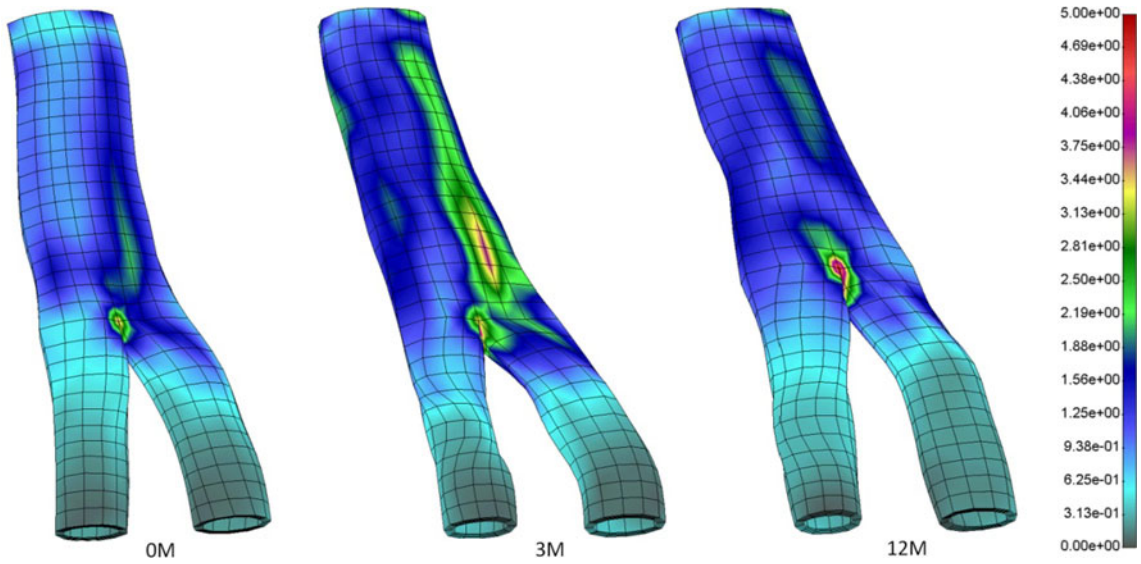

Fig. 5 Effective wall stress calculation for follow-up time baseline, 3 and 6 month for patient #1 (units 1 = 1e5 Pa)

Table 1 Computer model values for clinical data

Lumen	$\rho = 1{,}000$ kg/m^3	$\mu = 0.035$ (P)	$D_l = 3.8e^{-11}$ m^2/s	$U_{mean} = 0.5$ m/s	$P_{out} = 100$ mmHg	Co $= 2.5e^{-12}$ kg/m^3
Intima			$D_w = 1.6e^{-11}$ m^2/s	$r_w = -2.4e^{-4}$	$P_{med} = 100$ mmHg	
Inflammation	$d_1 = 1e^{-7}$ m^2/s	$d_2 = 1e^{-9}$ m^2/s	$d_3 = 1e^{-7}$ m^2/s	$k_1 = 2e^{-6}$ m^3/kg s	$\lambda = 25$ s^{-1}	$\gamma = 2$ s^{-1}

including the Kedem–Katchalsky equations to couple the transmural and transport within the lumen. The wall permeability was assumed to be a function of the WSS with lower permeability at low and oscillatory shear stress.

We described inflammatory process with reaction–diffusion PDE system. Our model starts with passive penetration of LDL in particular areas of the intima. We assumed that once in the intima, the part of LDL is immediately oxidized. When the oxidized LDL exceeds a threshold there is recruitment of monocytes. The incoming monocytes immediately differentiate into macrophages. Transformation of macrophages into foam cells contribute to the recruitment of new monocytes. It yields the secretion of a pro-inflammatory signal (cytokines), self-supportive inflammatory reaction. Newly formed foam cells are responsible for the local volume increase. Under a local incompressibility assumption, when foam cells are created, the intima volume is locally increasing. Volume changing of the wall has influence on the fluid lumen domain which means that complete coupling is achieved. The specific numerical procedures with ALE formulation were developed for this purpose. Our current approach is concentrated more on the process on plaque initiation and intimal thickening rather than a huge plaque progression and rupture. We did not take into account smooth muscle cell proliferation in this model and this will be investigated in our future study.

Fifty patients with carotid atherosclerotic disease are analyzed with MRI. Plaque components, i.e., lipid and fibrous tissue were manually delineated by two experienced MR readers.

Elastic material property of the wall was assumed. Mass-transfer equations for wall are considered to be stationary due to very slow process of plaque formation and development.

We examined patient data at three time points for the carotid artery, 0 (baseline), 3 and 12 months to make fitting of the parameter model for specific patient. Three-dimensional reconstruction was performed using high-resolution MRI system. Boundary conditions for the inlet velocity waveforms are measured from MR. Shear stress distribution mostly corresponds to the localisation of the plaque volume progression. Fluid–structure interaction was implemented to analyse effective wall stress distribution. We fitted patient data for plaque volume progression with growth functions which depend from fluid shear stress and arterial wall effective stress. Future research will go more into plaque structure for human data and additional different mechanisms for plaque progression and new concept to use exact geometrical model as in the isogeometric analysis [6].

Matching computed plaque location, composition and volume progression in time with clinical observations demonstrates a potential benefit for future prediction of this vascular disease using computer simulation.

We implemented a fitting procedure for plaque volume growing which takes into account change of the coordinates, shear stress as well as effective wall stress data from fluid–structure interaction calculation. Obviously low shear stress is not the only factor for local plaque development. Wall stress analysis as well as inflammation model with cell-level transformation and progression should be taken into account.

Acknowledgments This study was funded by a grant from FP7-ICT-2007 project (Grant agreement 224297, ARTreat) and grants from Serbian Ministry of Science III41007 and ON174028.

Appendix: Growth functions and the fitting procedure

For simulation of the plaque growth, the following procedure was used.

Step 1: Start from the original in geometry at $T1$;

Step 2: Set

$$
\begin{aligned}
f_{t1\_0}(i,j) &= f_{T1}(i,j)\\
f_{t1\_1}(i,j) &= f_{T1}(i,j) + (f_{T2}(i,j) - f_{T1}(i,j))/m\\
\tau_{t1\_0}(i,j) &= \tau_{T1}(i,j)\\
\tau_{t1\_1}(i,j) &= \tau_{T1}(i,j) + (\tau_{T2}(i,j) - \tau_{T1}(i,j))/m\\
\sigma_{t1\_0}(i,j) &= \sigma_{T1}(i,j)\\
\sigma_{t1\_1}(i,j) &= \sigma_{T1}(i,j) + (\sigma_{T2}(i,j) - \sigma_{T1}(i,j))/m
\end{aligned}
$$

Step 3: We use m time steps to go from $T1$ to $T2$ and n time steps to go from $T2$ to $T3$. This means that we use total $n+m$ time steps to go from $T1$ to $T3$. For $k = 1, \ldots n+m$ do the following:

- GF1:

$$
\begin{aligned}
f_{t1\_(k+1)}(i,j) = a_0(j) &+ a_1(j)\\
&\cdot (w(j)\cdot f_{t1\_k}(i,j) + (1-w(j))\cdot f_{t1\_0}(i,j))\\
&+ a_2(j)\cdot \left.\frac{\mathrm{d}f}{\mathrm{d}t}\right|_{T_{1\_k}}(i,j)\cdot \Delta t_k
\end{aligned}
$$

- GF2:

$$
\begin{aligned}
f_{t1\_(k+1)}(i,j) = a_0(j) &+ a_1(j)\cdot (w(j)\cdot f_{t1\_k}(i,j)\\
&+ (1-w(j))\cdot f_{t1\_0}(i,j))\\
&+ a_2(j)\cdot \left.\frac{\mathrm{d}f}{\mathrm{d}t}\right|_{T_{1\_k}}(i,j)\cdot \Delta t_k\\
&+ a_3(j)\cdot \tau_{t1\_k}(i,j) + a_4(j)\\
&\cdot \left.\frac{\mathrm{d}\tau}{\mathrm{d}t}\right|_{T_{1\_k}}(i,j)\cdot \Delta t_k
\end{aligned}
$$

- GF3:

$$
\begin{aligned}
f_{t1\_(k+1)}(i,j) = a_0(j) &+ a_1(j)\cdot (w(j)\cdot f_{t1\_k}(i,j)\\
&+ (1-w(j))\cdot f_{t1\_0}(i,j))\\
&+ a_2(j)\cdot \left.\frac{\mathrm{d}f}{\mathrm{d}t}\right|_{T_{1\_k}}(i,j)\cdot \Delta t_k + a_3(j)\\
&\cdot \tau_{t1\_k}(i,j) + a_4(j)\cdot \left.\frac{\mathrm{d}\tau}{\mathrm{d}t}\right|_{T_{1\_k}}(i,j)\\
&\cdot \Delta t_k + a_5(j)\cdot \sigma_{t1_k}(i,j)\\
&+ a_6(j)\cdot \left.\frac{\mathrm{d}\sigma}{\mathrm{d}t}\right|_{T_{1\_k}}(i,j)\cdot \Delta t_k
\end{aligned}
$$

where $\left.\frac{\mathrm{d}f}{\mathrm{d}t}\right|_{T_{1\_k}}(i,j) = \frac{f_{t1\_k}(i,j) - f_{t1\_(k-1)}(i,j)}{t_k - t_{k-1}}$, $\left.\frac{\mathrm{d}\tau}{\mathrm{d}t}\right|_{T_{1\_k}}(i,j) = \frac{\tau_{t1\_k}(i,j) - \tau_{t1\_(k-1)}(i,j)}{t_k - t_{k-1}}$, and $\left.\frac{\mathrm{d}\sigma}{\mathrm{d}t}\right|_{T_{1\_k}}(i,j) = \frac{\sigma_{t1\_k}(i,j) - \sigma_{t1\_(k-1)}(i,j)}{t_k - t_{k-1}}$ are derivatives of displacement, shear stress and solid stress, respectively, $\Delta t_k = t_{k+1} - t_k = \frac{T3-T1}{m+n}$ is a time step, f are x and y coordinates, τ are WSS values, σ are solid stress values of nodal points, $j = 1, 2, \ldots, 24$ is the slice number and i is the index for the points on each slice. $a_0(j), a_1(j), a_2(j), a_3(j), a_4(j), a_5(j), a_6(j)$ and $w(j)$ are coefficients of growth functions GF1, GF2 and GF3 to be determined in such a way to obtain the best match of calculated geometries and experimental geometries at times $T2$ and $T3$. Since we use m time steps to go from $T1$ to $T2$ and n time steps to go from $T2$ to $T3$, we compared f_{t1_m} with experimental geometry at time $T2$ and $f_{t1\_(m+n)}$ with experimental geometry at time $T3$. The previous formulas of growth functions are very similar with the formulas that Yang used in his paper [21].

Coefficients of the plaque volume growth functions (GF1, GF2 and GF3) $a_0, a_1, a_2, a_3, a_4, a_5, a_6$ and w are calculated, independently for all 24 slices using simplex optimization method, the method which does not involve derivative calculations, developed by John Nelder and Roger Mead [13]. We minimized sum of the squared errors between calculated and real geometry at times $T2$ and $T3$ for each of 24 slices.

$$
\begin{aligned}
\mathrm{ESS}(j) = &\sum_{i=1}^{N_j}\left(\left(x_{T2,i}(j) - \bar{x}_{T2,i}(j)\right)^2 + \left(y_{T2,i}(j) - \bar{y}_{T2,i}(j)\right)^2\right)\\
&+ \sum_{i=1}^{N_j}\left(\left(x_{T3,i}(j) - \bar{x}_{T3,i}(j)\right)^2 + \left(y_{T3,i}(j) - \bar{y}_{T3,i}(j)\right)^2\right)
\end{aligned}
$$

where N_j is the number of nodes for slice j, $x_{T2,i}(j)$, $y_{T2,i}(j)$, $x_{T3,i}(j)$, and $y_{T3,i}(j)$ are real x and y coordinates at time steps $T2$ and $T3$ for slice j, $\bar{x}_{T2,i}(j)$, $\bar{y}_{T2,i}(j)$, $\bar{x}_{T3,i}(j)$ and $\bar{y}_{T3,i}(j)$ are calculated x and y coordinates at time steps $T2$ and $T3$ for slice j.

The best results we obtained using growth function GF3 which takes into account wall shear and solid stress. Total squared error is calculated as:

$$\mathrm{ESS} = \sum_{j=1}^{24} \mathrm{ESS}(j)$$

Total squared errors for all growth functions are GF1 = 36.02, GF2 = 29.98, GF3 = 26.31.

Total squared error does not give a picture of how our model is really accurate, it only serves to compare the results obtained with different growth function. Because of that, we calculated mean relative percent error:

$$\mathrm{RE}(j) = \frac{1}{2N_j}\left(\sum_{i=1}^{N_j}\frac{\Delta P_{T2,i}(j)}{r_{T2,i}(j)} + \sum_{i=1}^{N_j}\frac{\Delta P_{T3,i}(j)}{r_{T3,i}(j)}\right) \times 100$$

$$\mathrm{RE} = \frac{1}{24}\sum_{j=1}^{24}\mathrm{RE}(j)$$

where $\Delta P_{T2,i}(j)$ and $\Delta P_{T3,i}(j)$ are distances between real and predicted position of ith point of jth slice at times $T2$ and $T3$. $r_{T2,i}(j)$ and $r_{T3,i}(j)$ are distances between real position of ith point and center of gravity for jth slice at times $T2$ and $T3$.

Mean relative percent errors for all growth functions are GF1 = 2.7 %, GF2 = 2.62 %, GF3 = 2.51 %. It can be observed that model which uses growth function GF3 is the most accurate. Mean relative percent errors for GF3 is 2.51 %, which means that distance between predicted position of point and real position of point is in average only 2.51 % of distance between real position of point and slice center of gravity. This seems to be very good result.

References

1. Ai L, Vafai K (2006) A coupling model for macromolecule transport in a stenosed arterial wall. Int J Heat Mass Transf 49:1568–1591
2. Chavent G (2002) Nonlinear least squares for inverse problems, nonlinear least squares for inverse problems theoretical foundations and step-by-step guide for applications, second print, Springer, New York
3. Filipovic N, Mijailovic S, Tsuda A, Kojic M (2006) An implicit algorithm within the arbitrary Lagrangian–Eulerian formulation for solving incompressible fluid flow with large boundary motions. Comp Methods Appl Mech Eng 195:6347–6361
4. Filipovic N, Meunier N, Boynard M, Kojic M, Fotiadis D (2010) A 3D computer simulation of plaque formation and development in coronary artery. In: Proceedings of ASME 2010 first global congress on nanoengineering for medicine and biology, NEMB2010, February 7–10, 2010 Houston
5. Filipovic N, Rosic M, Tanaskovic I, Milosevic Z, Nikolic D, Zdravkovic N, Peulic A. Fotiadis D, Parodi O (2011) ARTreat project: three-dimensional numerical simulation of plaque formation and development in the arteries. IEEE Trans Inf Technol Biomed. PMID: 21937352
6. Hughes TJR, Cottrell JA, Bazilevs Y (2005) Isogeometric analysis: CAD, finite elements, NURBS, exact geometry and mesh refinement. Comput Methods Appl Mech Eng 194:4135–4195
7. Kaazempur-Mofrad MR, Ethier CR (2001) Mass transport in an anatomically realistic human right coronary artery. Ann Biomed Eng 29:121–127
8. Kedem O, Katchalsky A (1958) Thermodynamic analysis of the permeability of biological membranes to non-electrolytes. Biochim Biophys 27:229–246
9. Kedem O, Katchalsky A (1961) A physical interpretation of the phenomenological coefficients of membrane permeability. J Gen Physiol 45:143–179
10. Kojic M, Filipovic N, Stojanovic B, Kojic N (2008) Computer modeling in bioengineering: theoretical background, examples and software. Wiley, Chichester
11. Libby P (2002) Inflammation in atherosclerosis. Nature 420(6917):868–874
12. Loscalzo J, Schafer AI (2003) Thrombosis and hemorrhage, 3rd edn. Lippincott Williams & Wilkins, Philadelphia
13. Nelder J, Mead R (1965) A simplex method for function minimization. Comput J 7:308–313
14. Olgac U, Kurtcuoglu V, Poulikakos (2008) Computational modeling of coupled blood-wall mass transport of LDL: effects of local wall shear stress. Am J Physiol Heart Circ Physiol 294:909–919
15. Quarteroni A, Veneziani A, Zunino P (2002) Mathematical and numerical modeling of the solute dynamics in blood flow and arterial walls. SIAM J Numer Anal 39:1488–1511
16. Ross R (1993) Atherosclerosis: a defense mechanism gone away. Am J Pathol 143:987–1002
17. Sadat U, Teng Z, Young VE, Zhu C, Tang TY, Graves MJ, Gillard JH (2010) Impact of plaque haemorrhage and its age on structural stresses in atherosclerotic plaques of patients with carotid artery disease: an MR imaging-based finite element simulation study. Int J Cardiovasc Imaging. doi:10.1007/s10554-010-9679-z
18. Stangeby DK, Ethier CR (2002) Computational analysis of coupled blood-wall arterial LDL transport. J Biomech Eng-T ASME 124:1–8
19. Tarbell JM (2003) Mass transport in arteries and the localization of atherosclerosis. Annu Rev Biomed Eng 5:79–118
20. Wada S, Koujiya M, Karino T (2002) Theoretical study of the effect of local flow disturbances on the concentration of low-density lipoproteins at the luminal surface of end-to-end anastomosed vessels. Med Biol Eng Comput 40:576–587
21. Yang C, Tang D, Atluri S (2010) Three-dimensional carotid plaque progression simulation using meshless generalized finite difference method based on multi-year MRI patient-tracking data. CMES 57:51–76
22. Zunino P (2002) Mathematical and numerical modeling of mass transfer in the vascular system. PhD thesis. EPFL, Lausanne